

A physics-informed neural network for quantifying the microstructure properties of polycrystalline Nickel using ultrasound data

Khemraj Shukla, Ameya D. Jagtap, James L. Blackshire,
Daniel Sparkman, and George Em Karniadakis

Abstract

We employ physics-informed neural networks (PINNs) to quantify the microstructure of a polycrystalline Nickel by computing the spatial variation of compliance coefficients (compressibility, stiffness and rigidity) of the material. The PINN is supervised with realistic ultrasonic surface acoustic wavefield data acquired at an ultrasonic frequency of 5 MHz for the polycrystalline material. The ultrasonic wavefield data is represented as a deformation on the top surface of the material with the deformation measured using the method of laser vibrometry. The ultrasonic data is further complemented with wavefield data generated using a finite element based solver. The neural network is physically-informed by the in-plane and out-of-plane elastic wave equations and its convergence is accelerated using adaptive activation functions. The overarching goal of this work is to infer the spatial variation of compliance coefficients of materials using PINNs, which for ultrasound involves the spatially varying speed of the elastic waves. More broadly, the resulting PINN based surrogate model shows a promising approach for solving ill-posed inverse problems, often encountered in the non-destructive evaluation of materials.

I. INTRODUCTION

In recent years, the availability of large datasets combined with sophisticated algorithms along with the exponential growth in computational power have led to an unprecedented surge of interest in machine

K. Shukla and A. D. Jagtap are with the Division of Applied Mathematics, Brown University, Providence, RI, 02906 USA e-mail: (khemraj_shukla@brown.edu, ameya_jagtap@brown.edu).

J. Blackshire and D. Sparkman are with Air Force Research Laboratory, Wright-Patterson AFB, OH, 45433, USA e-mail: (james.blackshire@us.af.mil, daniel.sparkman.1@us.af.mil).

G. Karniadakis is with the Division of Applied Mathematics and School of Engineering, Brown University, Providence, RI, 02906 USA and PNNL, Richland, WA, 99354 USA e-mail: (george_karniadakis@brown.edu).

learning techniques. Machine learning has been extensively used across the spectrum of disciplines ranging from the classification problem including speech recognition, natural language processing and computer vision, to complex regression problems like approximation of nonlinear and discontinuous functions. However, the applications of neural networks are less explored in the engineering fields. Physics-informed machine learning approaches define a new paradigm for bridging physical laws with observational data. Recently, such machine learning based techniques have attracted a lot of attention around the world, see [3] and references therein. In particular, Raissi *et al.* [3] proposed the physics-informed neural networks (PINNs) methodology, which can accurately solve the forward problem of inferring the solutions of governing physical laws, as well as inverse problems, where free parameters can be inferred or missing physics can be recovered using noisy, sparse and multi-fidelity scattered data sets. The PINN can easily incorporate all the given information such as governing differential/integro-differential equations, experimental/synthetic data etc. into the loss function, thereby recasting the original problem into an optimization problem. Incorporation of governing laws can drastically constrain the space of all admissible solutions. A major advantage of this method is providing a mesh-free algorithm for computation of the differential operators in the governing PDEs, which are approximated by automatic differentiation [4]. In this study, we explore the applicability of PINNs in solid mechanics, focusing on the quantification of microstructure in a material based on local elastic property variations.

The elastic properties of materials such as rigidity (c_{44} , c_{12}), and compressibility (c_{11}), computed at the microscale level, are utilized in ultrasound quantifying non-destructive sensing to characterize materials. The coefficients (c_{11} , c_{12} , and c_{44}) are known as elements of the stiffness tensor \mathbf{C} or compliance coefficients for linear elastic materials. These coefficients are primarily inferred from acoustic and ultrasonic signal data. In a typical measurement setting, an initiating pulse of ultrasonic energy is set to propagate along the surface of a material, which results in oscillation of particles described by the displacement vector $\mathbf{u} = [u_1, u_2, u_3]$. The \mathbf{u} is measured in the spatio-temporal domain as surface displacement of particles along the three orthogonal axes. In general, u_2 is measured experimentally by using an appropriate experimental setup, wherein the particle's displacements are recorded in the direction perpendicular to the plane-of-symmetry of the material. This approach is referred to as a surface acoustic wave (SAW) sensing method. In the literature, various experimental setups have been used to measure u_2 and subsequently used to infer the material properties. A detailed review of some of the methods used to acquire the displacement data was carried out by Xu *et al.* [10]. In addition, there are a number of methods that can be used to infer the microstructure of a material from the surface wavefield data (u_2). For example, the direction dependence of ultrasonic phase velocities, which are related to the mechanical properties of a material, have been used to quantify the anisotropy in materials [1], [2].

Seiner *et al.* [2] used this to study the symmetry of structures in polycrystalline Copper by analyzing the variation of anisotropy in different directions. In brief, methods to compute the microstructure properties of a material can be classified into groups (1) direct methods [12]–[14], and (2) inverse methods [10], [11]. Both direct and inverse methods are typically limited in handling materials based on single-crystal principles. However, Xu *et al.* [10] computed the elastic stiffness (c_{11}, c_{12}, c_{44}) by inverting the angular distribution of surface wave velocity by acoustic spectro-microscopy for each grain individually using an iterative approach.

Existing methods to infer the stiffness tensor are primarily based on analyzing the wavefield data represented by u_2 . However, the methods to analyze the full wavefield data defined by vector \mathbf{u} have not been fully explored. Therefore, none of the existing methods address an holistic approach of dealing with the entire wavefield data set to compute the stiffness tensor or microstructure properties. Additionally, the wavefield data acquired experimentally or numerically are often sparse and high-dimensional in nature, and therefore, careful attention is required to express these data while inferring the material properties.

The first successful implementation of PINNs in non-destructive evaluation was carried out by Shukla *et al.* [5], where they solved the problem of detecting and characterizing a surface crack in a metal plate of Aluminum alloy. The present study is motivated by the work of Shukla *et al.* [5] but the primary objective here is to quantify the microstructure properties of polycrystalline Nickel from ultrasound non-destructive evaluation measurement data. The primary significance of this work is in the performance of turbine engine materials, where microstructure states play an important role. In this work, we employed PINNs to quantify the microstructure properties by computing \mathbf{C} . The governing equations are defined by two decoupled system of partial differential equations (PDEs). Each set of PDEs expresses in-plane (u_1, u_3) and out-of-plane particle displacement (u_2) explicitly. The grain distribution in the polycrystalline Nickel plate attributes to different material properties defined by the local stiffness tensor (compliance coefficients) \mathbf{C} . Wavefield data over the surface of the metal plate is acquired for different ultrasonic frequencies, spatial resolutions, grains statistics, and grain orientation states by using the laser vibrometry sensing method [8]. The experimental data only generates out-of-plane displacement u_2 , therefore the experimental data is further augmented with the numerical data generated using a finite element based solver and synthetic microstructure states generated using the DREAM3D software package [16]. In this paper, we show that PINNs can compute c_{44} from the experimental data and c_{11}, c_{12} from the numerical data. Furthermore, we also show that by using only 10-20 % of the total acquired data along with usage of the adaptive activation functions [6], the objective of computing the stiffness tensor \mathbf{C} can be successfully achieved. The conventional solvers often face difficulties to solve ill-posed inverse problems, but PINNs can be easily employed to solve such problems accurately and efficiently. Our approach is novel as

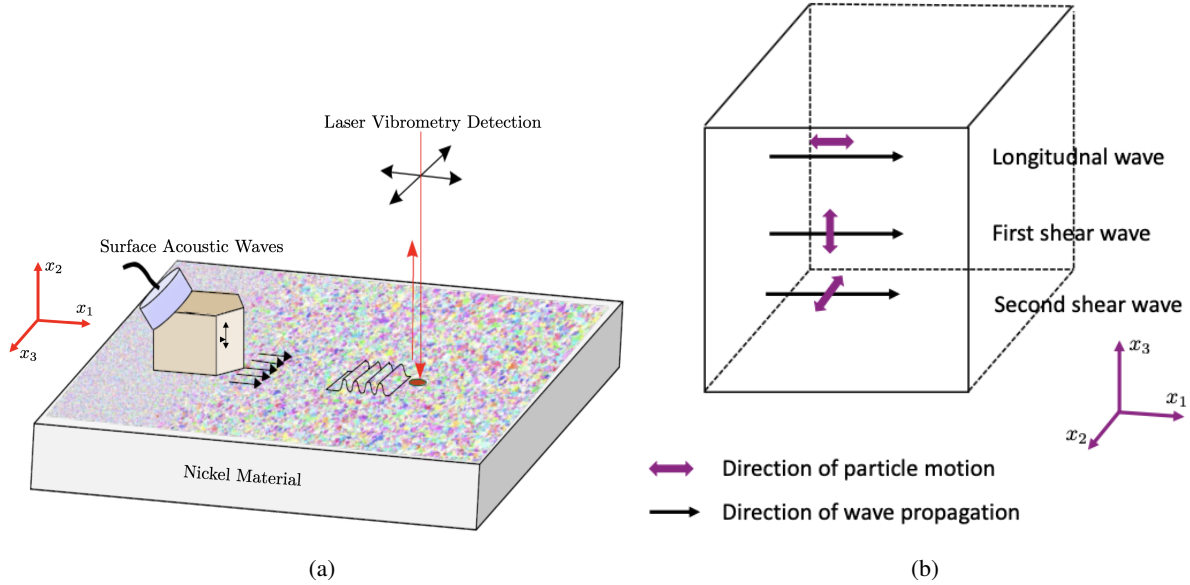


Fig. 1. (a) Experimental setup for measuring u_2 on a metal surface. The color patches on surface represent polycrystalline grain orientation variations. (b) Types of waves and particle motions generated due to propagation of ultrasonic waves.

we formulate mathematical models for in- and out-of plane particle displacements, and implement such models in PINNs to solve the inverse problem where the stiffness tensor of polycrystalline material is inferred using only the displacement data obtained from the experiment as well as corresponding auxiliary FEM simulations.

This paper is organized as follows. Section II deals with the definition of the problem and the physics of in-plane and out-of-plane particle motion with appropriate and necessary mathematical concepts. In Section III, we describe the PINN methodology in detail and then explain its application for the quantification of microstructure states. Section IV provides the details of pre-processing of the experimental data, followed by section V where all the results are discussed in detail. Finally, we summarize our findings in section VI.

II. PROBLEM DEFINITION

In this section, we will describe the physics of elastic wave propagation for in-plane and out-of-plane particle motion along with the details on the corresponding data sets. Prior to that, we will briefly describe the definition of the constitutive relations and the specific definitions for polycrystalline Nickel. Polycrystalline Nickel exhibits a cubic symmetry and its microstructure is primarily defined by the elements of stiffness tensor, i.e., c_{11} , c_{12} and c_{44} . Here, c_{11} represents the linear combination of compressibility and rigidity, whereas c_{12} and c_{44} define the rigidity of the materials. These coefficients

define the strain in a continuum represented by a control volume whose surfaces are parallel to the coordinate system represented by (x_1, x_2, x_3) . The relation between stress and strain is expressed as [15]

$$\boldsymbol{\sigma} = \begin{bmatrix} c_{11} & c_{12} & c_{12} & 0 & 0 & 0 \\ c_{12} & c_{11} & c_{12} & 0 & 0 & 0 \\ c_{12} & c_{12} & c_{11} & 0 & 0 & 0 \\ 0 & 0 & 0 & c_{44} & 0 & 0 \\ 0 & 0 & 0 & 0 & c_{44} & 0 \\ 0 & 0 & 0 & 0 & 0 & c_{44} \end{bmatrix} \boldsymbol{\epsilon}, \quad (1)$$

where $\boldsymbol{\sigma} = [\sigma_{11}, \sigma_{22}, \sigma_{33}, \sigma_{23}, \sigma_{13}, \sigma_{12}]^T$ and $\boldsymbol{\epsilon} = [\epsilon_{11}, \epsilon_{22}, \epsilon_{33}, 2\epsilon_{23}, 2\epsilon_{13}, 2\epsilon_{12}]^T$ are the stress and strain tensors, respectively.

The subscripts of notations in (1) follow the Voigt notation [15]. For example, in σ_{11} the first index specifies the direction in which the stress component acts, i.e., x_1 , while the second index identifies the orientation of the surface upon which it is acting (which is also x_1). The same definition applies to c_{11} , c_{12} and c_{44} and the components of the tensors. Elements of strain tensor ($\boldsymbol{\epsilon}$) are expressed in terms of the particle displacements $\mathbf{u} = [u_1, u_2, u_3]$, which are the measured and simulated data to be used for the quantification of the microstructure. The following is the expression for strain component applicable in the context of this study

$$\epsilon_{11} = \frac{\partial u_1}{\partial x_1}, \quad \epsilon_{33} = \frac{\partial u_3}{\partial x_3}, \quad \text{and} \quad \epsilon_{13} = \frac{1}{2} \left(\frac{\partial u_1}{\partial x_3} + \frac{\partial u_3}{\partial x_1} \right). \quad (2)$$

In Figure 1a, we describe the experimental setup for measuring the particle displacement at the surface of the material by using the propagation of ultrasonic surface acoustic waves. An impulse excitation centered about 5 MHz was induced on the surface of the material. As the wave traverses, energy in the wave causes particles to oscillate. The direction of particle motion vis-a-vis energy propagation is affected by the elastic properties of the material. Figure 1 (b) shows the three cases of particle displacement and energy propagation. The first case corresponds to the compressive-extension motions where the particle motion is along the direction of energy propagation and represents longitudinal waves. The second case defines the particle motion being orthogonal to the direction of energy propagation, where particles polarized in the vertical plane represent the first shear wave. Finally, the last case corresponds to particle motions orthogonal to the direction of energy propagation with particles polarized in the horizontal plane representing the second shear wave. We denote the velocity of longitudinal wave, first shear wave, and second shear wave as v_p , v_{s_1} and v_{s_2} , respectively. The particle displacement corresponding to longitudinal, first, and second shear waves are denoted as u_1 , u_3 , and u_2 , respectively. To measure u_2 , we have used the setup shown in Figure 1 (a) and the wavefield imaging method [8]. In practice, the

wavefield imaging method uses a scanning laser vibrometry system to detect displacement fields on a material surface with nanometer precision. The laser vibrometer uses a focused laser beam and coherent light interference principles to convert phase interference of the light into particle displacement surface deformation measurement. For the present study, a contact wedge surface acoustic waves transducer was held stationary on the material surface to generate the ultrasound field Figure 1a, while the laser vibrometry beam was scanned in the (x_1, x_3) plane [8]. Repetitions of the ultrasonic excitation for different vibrometry detection points (x_1, x_3) enables the collection of time series data (displacement amplitude vs time signals) at discrete (x_1, x_3) spatial locations and captured at regularized grid points. These measurements are stored as a collection of time-evolving snapshots of $u_2(x_1, x_3, t)$ data showing important details of the ultrasound wave propagation and scattering phenomena occurring between the ultrasound field and the local material features (e.g. grain boundaries).

In a 2D plane-of-symmetry $(x_1 - x_3)$, particle displacement u_2 , contained in a plane perpendicular to $(x_1 - x_3)$ plane ($\partial x_2 = 0$), is expressed as [15]

$$\rho(\mathbf{x}) \frac{\partial^2 u_2}{\partial t^2} = \left(\frac{\partial \sigma_{12}}{\partial x_1} + \frac{\partial \sigma_{23}}{\partial x_3} \right), \quad (3)$$

where $\sigma_{12} = c_{44}(\mathbf{x}) \frac{\partial u_2}{\partial x_3}$ and $\sigma_{23} = c_{44}(\mathbf{x}) \frac{\partial u_2}{\partial x_1}$, $\rho(\mathbf{x})$ is density of material, $x_1, x_3 \in \Omega \subset \mathbb{R}^2$ and $t \in [0, T]$. Substituting the definition of σ_{12} and σ_{23} in (3), we recover

$$\frac{\partial^2 u_2}{\partial t^2} = 2\hat{c}_{44} \frac{\partial^2 u_2}{\partial x_1 \partial x_3}, \quad (4)$$

where $\hat{c}_{44} = \frac{c_{44}(\mathbf{x})}{\rho(\mathbf{x})}$.

To compute the c_{11} and c_{12} , u_1 and u_3 are generated numerically by using the DREAM-3D package [16]. The particle displacement u_1 and u_3 in the (x_1, x_3) plane are defined by following set of PDEs [15]

$$\begin{aligned} \frac{\partial^2 u_1}{\partial t^2} &= \frac{\partial \sigma_{11}}{\partial x_1} + \frac{\partial \sigma_{13}}{\partial x_3}, \\ \frac{\partial^2 u_3}{\partial t^2} &= \frac{\partial \sigma_{13}}{\partial x_1} + \frac{\partial \sigma_{33}}{\partial x_3}, \end{aligned} \quad (5)$$

where $\sigma_{11} = \hat{c}_{11} \frac{\partial u_1}{\partial x_1} + \hat{c}_{12} \frac{\partial u_3}{\partial x_3}$, $\sigma_{33} = \hat{c}_{12} \frac{\partial u_1}{\partial x_1} + \hat{c}_{11} \frac{\partial u_3}{\partial x_3}$ and $\sigma_{13} = \hat{c}_{44} \left(\frac{\partial u_3}{\partial x_1} + \frac{\partial u_1}{\partial x_3} \right)$ with $\hat{c}_{ij} = \frac{c_{ij}(\mathbf{x})}{\rho(\mathbf{x})}$.

The speed of longitudinal, first shear and second shear waves in the Nickel is expressed as [17]

$$v_{p_1} = \sqrt{\frac{c_{11}}{\rho}}, \quad v_{s_1} = \sqrt{\frac{c_{11} - c_{12}}{\rho}}, \quad \text{and} \quad v_{s_2} = \sqrt{\frac{c_{44}}{\rho}} \quad (6)$$

Thus, in this paper we will be addressing the following problem. Given the displacement vector $\mathbf{u} = [u_1, u_2, u_3]$ for polycrystalline Nickel, we have to compute c_{11} , c_{12} and c_{44} (or v_{p_1} , v_{s_1} and v_{s_2}) from the neural networks informed by the physics defined in equations (4) and (5).

III. PHYSICS-INFORMED NEURAL NETWORK

In this section we will describe the design of the PINN to compute \hat{c}_{11} , \hat{c}_{12} and \hat{c}_{44} . Prior to that, we shall briefly explain the mathematical setup for the fully-connected feed-forward neural network (FFNN).

A. Neural network - Mathematical setup

We have chosen a FFNN of depth D with an input layer, $D - 1$ hidden layers and an output layer. In the k^{th} hidden layer, the number of neurons is denoted by N_k . Each hidden layer receives an affine transformed output $\mathbf{x}^{k-1} \in \mathbb{R}^{N_{k-1}}$ from the previous layer. The affine transformation is expressed as

$$\mathcal{L}_k(\mathbf{x}^{k-1}) := \mathbf{w}^k \mathbf{x}^{k-1} + \mathbf{b}^k. \quad (7)$$

In the k^{th} layer of the network, the weights $\mathbf{w}^k \in \mathbb{R}^{N_k \times N_{k-1}}$ and the biases $\mathbf{b}^k \in \mathbb{R}^{N_k}$ are initially chosen from *independent and identically distributed (i.i.d)* samplings. The nonlinear activation function $\Phi(\cdot)$ is applied to $\mathcal{L}_k(\mathbf{x}^{k-1})$ component-wise prior to sending it as input to the next layer. The activation function at the output layer is an identity function. Thus, the final neural network representation is expressed as

$$\mathbf{u}_\Theta(\mathbf{x}) = (\mathcal{L}_k \circ \sigma \circ \mathcal{L}_{k-1} \circ \dots \circ \sigma \circ \mathcal{L}_1)(\mathbf{x}), \quad (8)$$

where $\mathbf{u}_\Theta(\mathbf{x})$ is the output of the neural network and the operator \circ is the composition operator, $\Theta = \{\mathbf{w}^k, \mathbf{b}^k, a\}_{k=1}^D$ represents all the trainable parameters in the network including the slope of the activation function defined as a . Adaptive activation functions are shown to accelerate the training of the deep as well as physics-informed neural networks by introducing the trainable parameters in the activation function, which can be optimized along with the other parameters in the neural networks. We employ global adaptive activation function, see [6], [7], [9] for more details.

B. PINNs for computing \hat{c}_{11} , \hat{c}_{12} and \hat{c}_{44}

In this section, we shall explain the architecture of the neural networks informed by governing equations (equations (3) and (5)), which will infer \hat{c}_{11} , \hat{c}_{12} and \hat{c}_{44} .

- **PINN for \hat{c}_{44} :**

First, we will define the construction of PINN to compute \hat{c}_{44} from the particle displacement data u_2 . We define the residual f_2 from (4) as

$$f_2 := \frac{\partial^2 u_2}{\partial t^2} - 2\hat{c}_{44} \left(\frac{\partial^2 u_2}{\partial x_1 \partial x_3} \right), \quad (9)$$

and proceed by approximating $u_2(t, x)$ and $\hat{c}_{44}(\mathbf{x})$ with two separate deep neural networks as shown in Figure 2 with blocks annotated with *Neural Network 1* and *Neural Network 2*. The reason behind

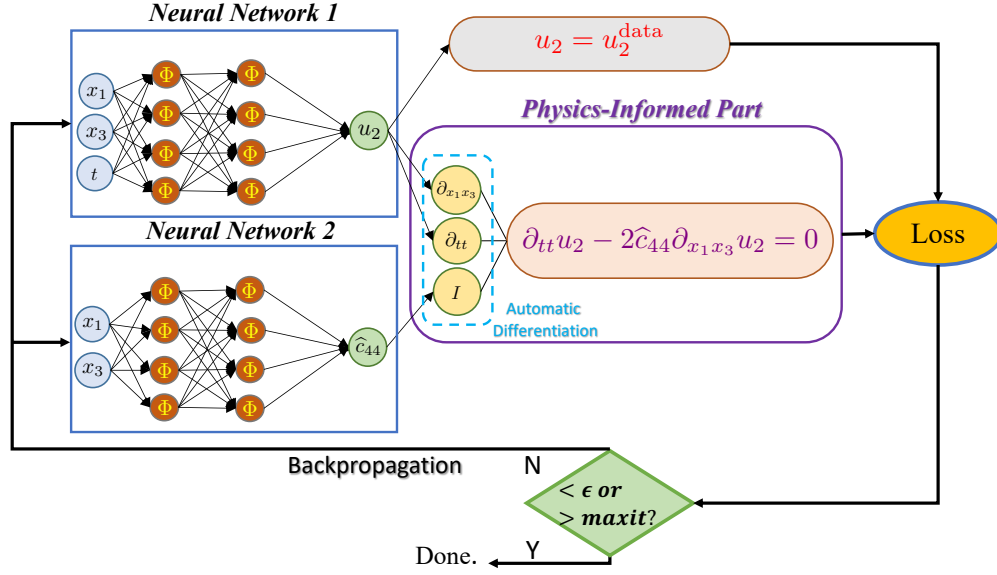


Fig. 2. Physics-informed neural network to compute \hat{c}_{44} , described in equation (3).

choosing the two separate neural networks to learn u_2 and \hat{c}_{44} is their dependencies on different input variables, which for u_2 is (x_1, x_3, t) whereas for \hat{c}_{44} is (x_1, x_3) . It is important to note that during the training procedure both the networks are trained simultaneously. The output of the neural networks not only satisfies the given data but also the governing equation as shown by the physics-informed part. The spatio-temporal derivatives in the governing equation (9) are computed by using the automatic differentiation [4]. The PINN algorithm aims to learn a surrogate $u_2 = u_{2_\Theta}$ for predicting the solution of (4). The PINN loss function is given as

$$J_{\hat{c}_{44}}(\Theta) = \lambda_{u_2} MSE_{u_2} + \lambda_{f_2} MSE_{f_2}, \quad (10)$$

where the data loss is given by $MSE_{u_2} = \frac{1}{N_{u_2}} \sum_{i=1}^{N_{u_2}} |u_{2_\Theta}(\mathbf{x}_{u_2}) - u_2^{\text{data}}(\mathbf{x}_{u_2})|^2$, and the residual loss is

$MSE_{f_2} = \frac{1}{N_{f_2}} \sum_{i=1}^{N_{f_2}} |f_2(\mathbf{x}_{f_2})|^2$. The parameter $\lambda_{u_2}, \lambda_{f_2} > 0$ is the penalty parameter, which helps in achieving the fast convergence. Here, \mathbf{x}_{u_2} and \mathbf{x}_{f_2} represent the spatio-temporal locations of training data (experimentally measured u_2) and the residual points, respectively. Our objective is to achieve the optimal parameters of neural network for which the loss function defined in (10) is minimized.

Thus, the definition of the resulting optimization problem is expressed as

$$\Theta^* = \arg \min_{\Theta \in \mathcal{V}} J_{\hat{c}_{44}}(\Theta), \quad (11)$$

where \mathcal{V} is the parametric space. The stochastic gradient descent (SGD) method is the widely used optimization method. In SGD, a small set of points is randomly sampled to find the direction of the gradient in every iteration. The SGD algorithm works well to avoid bad local minima during training of DNN under the one point convexity property. In particular, we shall use the Adam optimizer, which is one of the version of SGD, followed by the L-BFGS optimizer.

- **PINNs for \hat{c}_{11} and \hat{c}_{12} :**

For constructing the parameters \hat{c}_{11} and \hat{c}_{12} , we shall use the already computed \hat{c}_{44} from the previously defined PINNs. The residuals for equation 5 is expressed as

$$\begin{aligned} f_1 &:= \frac{\partial^2 u_1}{\partial t^2} - \left[\hat{c}_{11} \frac{\partial^2 u_1}{\partial x_1^2} + \hat{c}_{12} \frac{\partial^2 u_3}{\partial x_1 \partial x_3} + \hat{c}_{44} \left(\frac{\partial^2 u_3}{\partial x_3 \partial x_1} + \frac{\partial^2 u_1}{\partial x_3^2} \right) \right] \\ f_3 &:= \frac{\partial^2 u_3}{\partial t^2} - \left[\hat{c}_{12} \frac{\partial^2 u_1}{\partial x_1 \partial x_3} + \hat{c}_{11} \frac{\partial^2 u_3}{\partial x_3^2} + \hat{c}_{44} \left(\frac{\partial^2 u_3}{\partial x_1^2} + \frac{\partial^2 u_1}{\partial x_1 \partial x_3} \right) \right] \end{aligned} \quad (12)$$

The PINN consists of three networks where the first network approximates the data $u_1(\mathbf{x})$ and $u_3(\mathbf{x})$. The second and third networks approximate \hat{c}_{11} and \hat{c}_{12} , respectively. The combination of these three networks approximates u_1 and u_3 , which are approximated at the sampled residual points and fed to the residuals defined in (12). Therefore, the loss function is defined as

$$J_{\hat{c}_{11}, \hat{c}_{12}}(\Theta) = \lambda_{u_1} MSE_{u_1} + \lambda_{u_3} MSE_{u_3} + \lambda_{f_1} MSE_{f_1} + \lambda_{f_3} MSE_{f_3}, \quad (13)$$

where MSE_{u_1} , MSE_{u_3} , MSE_{f_1} and MSE_{f_3} correspond to mean square error of u_1 , u_3 , f_1 and f_3 , respectively. Again, the parameters λ_{u_1} , λ_{u_3} , λ_{f_1} and λ_{f_3} are all positive penalty parameters. The \hat{c}_{11} and \hat{c}_{12} can be recovered by optimizing the loss function $J_{\hat{c}_{11}, \hat{c}_{12}}(\Theta)$ as discussed before.

IV. PRE-PROCESSING OF EXPERIMENTAL DATA

In this study, we have analyzed two sets of wavefield data acquired over the Nickel metal surface of dimension 10 mm \times 10 mm with (50 \times 50) and (400 \times 400) grids. Wavefield data for both grids are based on the collection of 384 time snapshots (with time step $dt = 0.02 \mu s$) stored in a 3D array of size $[N_{x_1}, N_{x_3}, N_t] = [50, 50, 384]$ and $[N_{x_1}, N_{x_3}, N_t] = [400, 400, 384]$, respectively. To filter out these very small energy events, we employed the method of *principal component analysis (PCA)*, which is a method for extracting the variance structure from the high-dimensional data and project the data into a subspace such that the variance of projected data is maximized. The PCA based analysis confirms that the wavefield data for (400 \times 400) has some high-frequency and very small energy events, which will result in a slow convergence of PINNs due to spectral bias in the neural network, i.e., the highest frequencies are learned last and hence it takes very long time to resolve them [22].

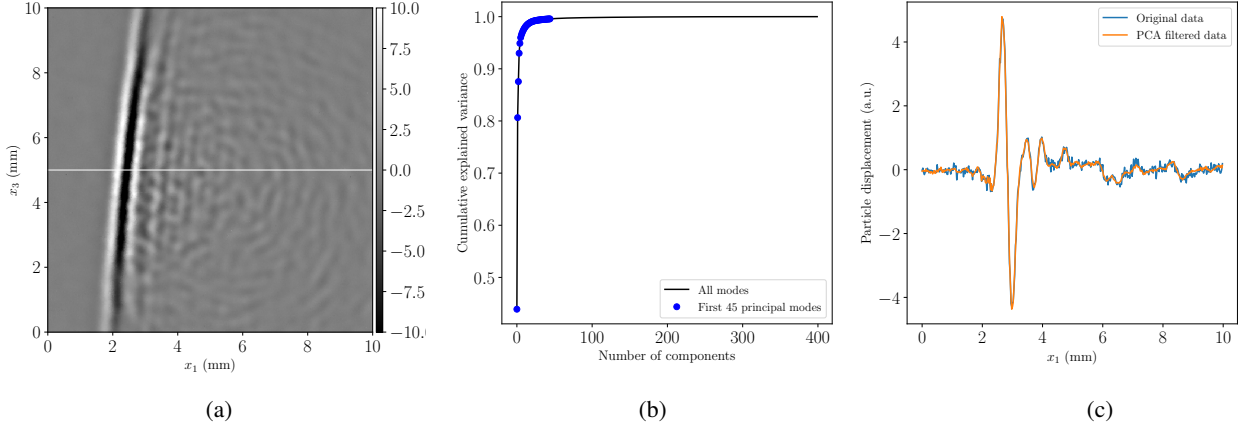


Fig. 3. Pre-processing of wavefield data acquired at 5 MHz. (a) represents a time snapshot ($t = 3.84 \mu s$) of experimental raw wavefield data u_2 , acquired at frequency of 5 MHz with $N_{x_1} = N_{x_3} = 400$. (b) represents cumulative explained variance of (a) (plotted in black solid line), which also shows the first 45 modes containing the significant energy (plotted in blue solid markers). (c) represents a comparison between raw and filtered trace extracted at $x_3 = 5$ mm marked by the solid white line in Figure 3a.

The first step in the implementation of PCA is to compute the singular value decomposition. We represent a time snapshot with \mathbf{X} and its singular value decomposition as

$$\mathbf{X} = \mathbf{U}\mathbf{S}\mathbf{V}^\top, \quad (14)$$

where \mathbf{U} is a unitary matrix and \mathbf{S} is the diagonal matrix of singular values s_i and \mathbf{V} is matrix of eigenvector of covariance matrix $\frac{\mathbf{X}^\top \mathbf{X}}{(N_{x_1} - 1)}$. It is to be noted that \mathbf{X} does not need to be a centered matrix, i.e., symmetric and idempotent.

In Equation (14), the term $\mathbf{U}\mathbf{S}$ represents principal components and \mathbf{V} represent principal direction.

To filter out the data corresponding to low energy principal components, a ratio of the variance of that principal component and the sum of the variances of all individual principal components is computed. Hence, the filtering process employs the zeroing-out of one or more of the smallest principle components by preserving the maximum data variance. Figure 3a shows a time snapshot of raw wavefield data (u_2) at a representative time $t = 3.84 \mu s$. Figure 3b shows the ratio between the variance of that principal component and the sum of variances of all individual principal components for the wavefield shown in Figure 3a. Figure 3b shows that the dominant modes of energy are contained only in the first 45 principal components (blue solid markers), and therefore we filtered out the remaining components. A comparison between filtered and non-filtered traces is shown in Figure 3c. The trace is extracted along the solid white horizontal line as shown in Figure 3a. Figure 3b clearly shows that PCA is very effective

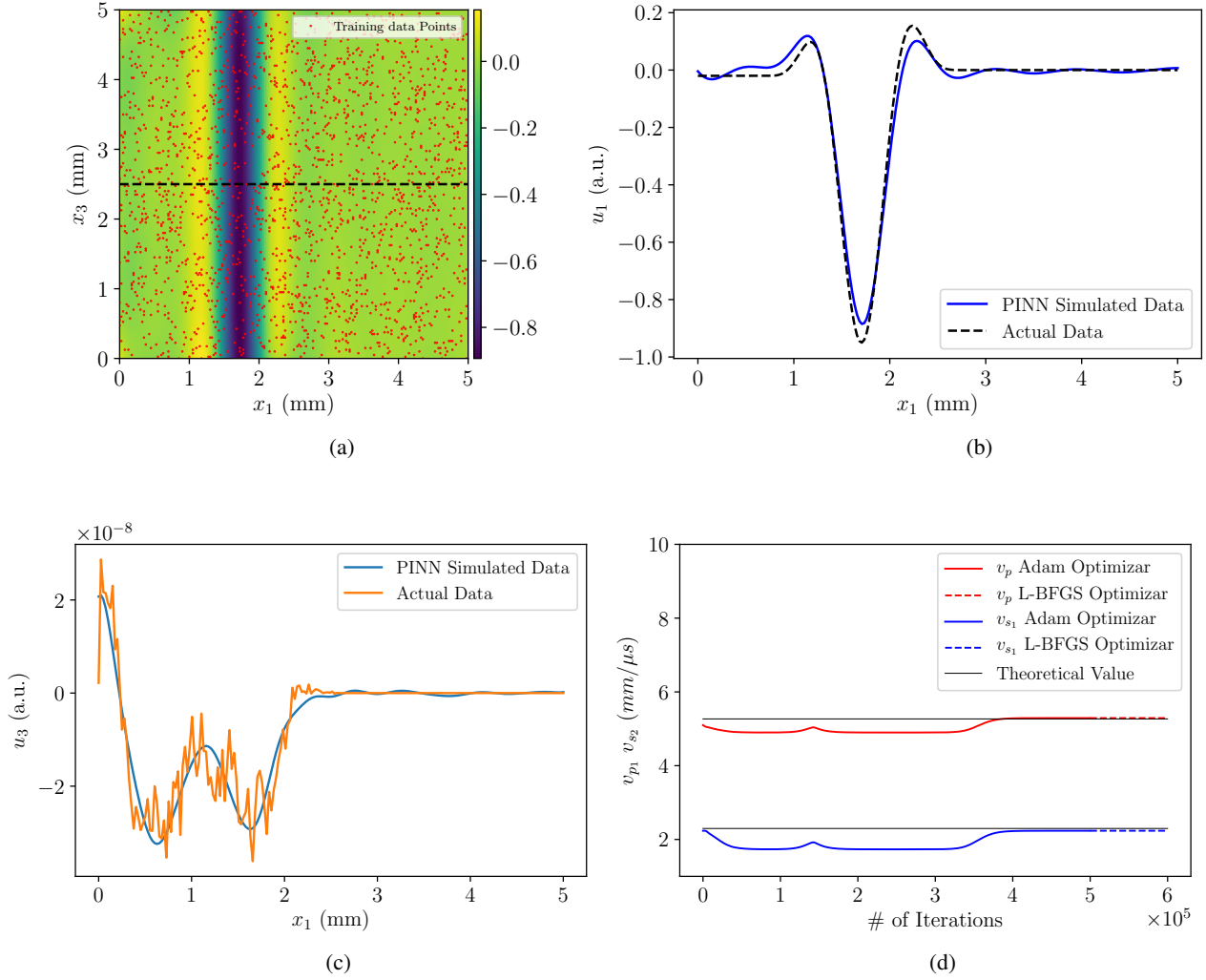


Fig. 4. Results from training of PINNs for data generated from finite element modeling approach by solving the elastic wave equation for u_1 and u_3 . The data is simulated for a single-crystal Nickel. (a) shows a time snapshot of u_1 at $t = 0.52 \mu s$. Red solid dots represent the location of data points sampled for the training of PINNs. (b) shows a comparison of actual and PINN simulated u_1 along a black dashed horizontal line in (a). (c) shows a comparison of actual and PINN simulated u_3 along a black dashed horizontal line in (a), and (d) shows the velocity of longitudinal (v_{p1}) and the first shear wave (v_{s1}) along with the actual velocities plotted in solid black line.

in filtering out unwanted high-frequency and low energy noises. The choice of first 45 components is very conservative to avoid the loss of any important information. The PCA has been applied to each time snapshot individually on the dataset acquired for 400×400 grid points. However, the PCA has not been applied on 50×50 datasets due to the uniform distribution of energy over all the principal components of the time snapshots.

TABLE I
 c_{11} AND c_{12} OF SINGLE-CRYSTAL NICKEL

	c_{11} (GPa)	c_{12} (GPa)
Actual values	257	153
PINN computed values	249.20	160.20
Relative L_2 errors	3%	4%

TABLE II
 v_{s_2} AND c_{44} OF POLYCRYSTALLINE NICKEL WITH VARIATIONS IN THE WIDTH AND DEPTH OF THE NETWORK.

Width (N), Depth (L)	v_{s_2} $\text{mm}\mu\text{s}$ (max, min)	c_{44} GPa (max, min)
N=50, L=2	(2.98, 2.99)	(79.04, 79.57)
N=50, L=3	(2.98, 2.99)	(79.04, 79.57)
N=50, L=4	(2.96, 2.99)	(77.98, 79.57)
N=50, L=5	(2.94, 3.00)	(76.93, 80.10)
N=50, L=6	(2.95, 3.00)	(77.45, 80.10)
N=10, L=6	(2.98, 2.99)	(79.04, 79.57)
N=20, L=6	(2.98, 3.09)	(79.04, 80.63)
N=30, L=6	(2.94, 3.00)	(76.93, 80.10)
N=40, L=6	(2.94, 3.00)	(76.93, 80.10)
N=50, L=6	(2.95, 3.00)	(77.45, 80.10)

V. RESULTS

In this section, we will discuss the efficacy of PINN, described in Section 2, in quantifying the microstructure of polycrystalline Nickel. We primarily considered the two cases, first, we validated the results of PINN by computing the \hat{c}_{11} and \hat{c}_{12} for a single-crystal Nickel. In the second case, the spatial

TABLE III
 HYPER-PARAMETERS OF THE NEURAL NETWORK AND THE TRAINING DATA DETAILS

Hyperparameters used in this study and the details of training data						
Results in	Depth	Width	Number of iterations ($\times 10^5$)	Activation function	Learning rate	% of spatial data used
Figure 4	2	32	2	sin	$1e - 4$	40%
Figure 5 NN1	6	50	2	sin	$2e - 4$	20%
Figure 5 NN2 (\hat{c}_{44})	2	16	2	sin	$2e - 4$	20%

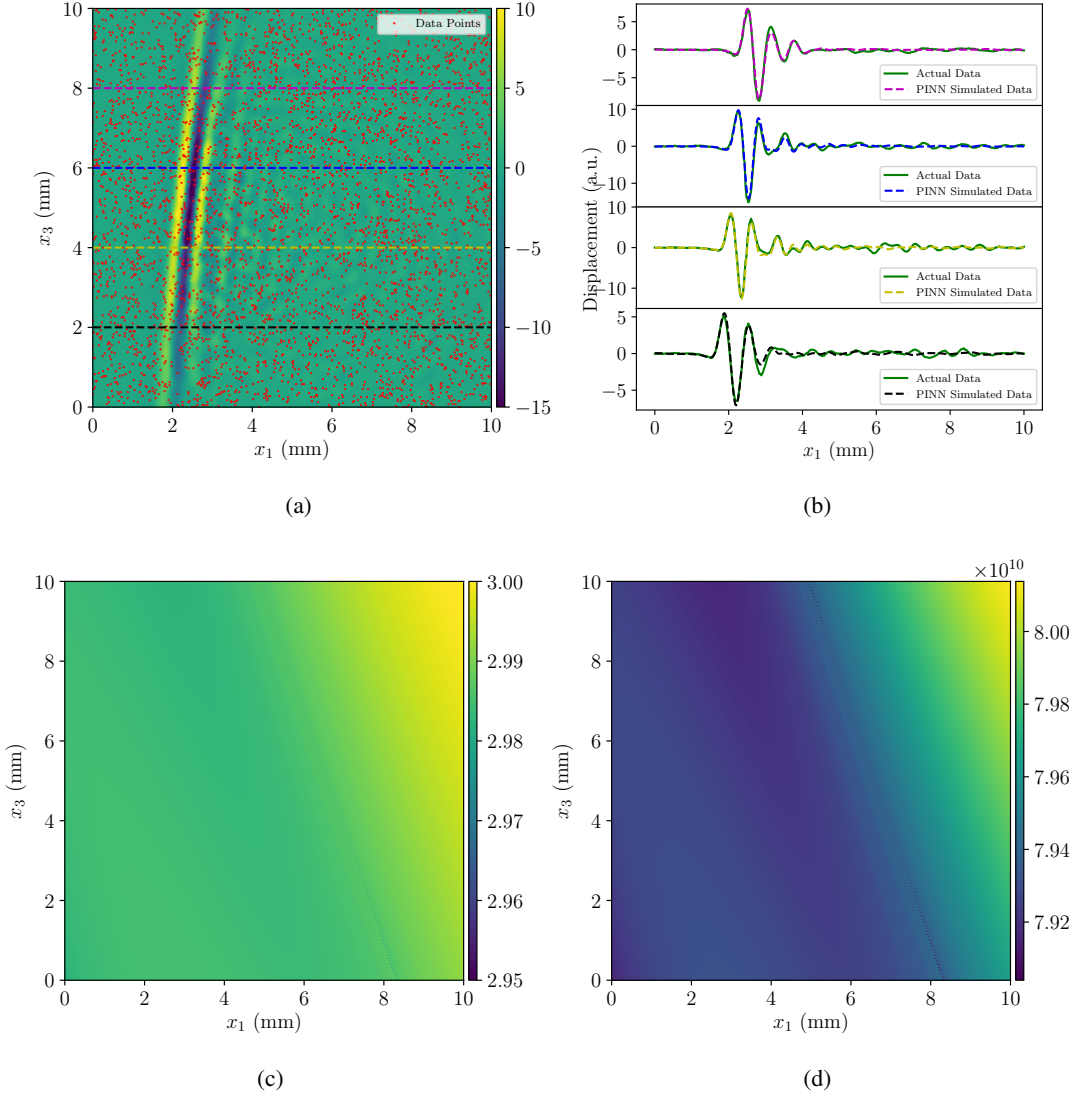


Fig. 5. Results from training of PINN for wavefield data (u_2) acquired over the surface of a metal plate of dimension (10 mm \times 10 mm) with $(N_{x_1}, N_{x_3}) = (400 \times 400)$ spatial grid points. (a) shows a time snapshot of PCA filter data at $t = 3.84 \mu s$ overlaid with red colored dots representing the location of training data points for PINNs. (b) shows a comparison between the traces of actual and PINN simulated data along the color lines shown in (a). Color of traces corresponds to the color and the location of lines in (a). (c) shows the speed of space-dependent second shear wave mode $v_{s_2}(x_1, x_3)$. Spatial variation of speed confirms the distribution of polycrystals in the material. (d) shows the spatial variation of c_{44} .

variation of \hat{c}_{44} is computed for the polycrystalline Nickel using PINN.

A. PINN for single-crystal Nickel

To validate the applicability of PINN for microstructure quantification, computation of \hat{c}_{11} and \hat{c}_{12} is performed for an isotropic single-crystal Nickel of dimension 5 mm \times 5 mm with crystallographic

orientation of $(0, 0, 0)$. The crystallographic orientation describes the angle between the plane described by the Cartesian system and plane-of-symmetry of the material. The stiffness tensor \mathbf{C} for the numerical simulation is adopted from Xu *et al.* [10]. The data for u_1 and u_3 were generated numerically by solving the elastic wave equation [13] for a plane wave of 5 MHz as an initial condition. The spatial and temporal grid size for discretization are $[\Delta x_1, \Delta x_3, \Delta t] = [0.025 \text{ mm}, 0.025 \text{ mm}, 0.40 \text{ ns}]$. For training of the PINN, we considered 14 time snapshots representing the time duration between $0.4 - 0.57 \mu\text{s}$, and each time snapshot is spatially sampled with 40% data. Figure 4a represents one of the time snapshots at $t = 0.52 \mu\text{s}$ overlaid with the red solid dots representing the training data points sampled in an *i.i.d* (independent and identical distribution) way. Thereafter, PINN simulation is performed, as described in Section 2, to recover the full field of u_1 and u_3 , \hat{c}_{11} and \hat{c}_{12} . The hyper-parameters of the neural networks are given in Table III.

The values of λ_{u_1} , λ_{u_2} , λ_{f_1} , and λ_{f_3} in (13) are taken as 50, 20, 1, and 1, respectively. Figures 4b and 4c show a comparison between the actual and PINN simulated solutions of u_1 and u_3 , extracted along the black dashed line shown in Figure 4a. The comparison of u_1 shows a very good agreement. Amplitudes of u_3 are very small ($O(10^{-8})$) and are represented by a very high frequency spatial variation as shown in Figure 4c. The small amplitudes of u_3 are defined by the wave vector defining the direction of propagation of wave energy, which is directed towards x_1 for this case. Therefore, a very small fraction of energy is responsible for causing the oscillation in x_3 direction, resulting in the small scales of u_3 . However, pairing PINNs with appropriate scaling factor results into a reasonable approximation of u_3 as shown in Figure 4c. Figure 4d represents v_{p_1} and v_{s_1} recovered from PINN. In Figure 4d, the solid and dashed portions of red and blue lines correspond to Adam and L-BFGS optimizer, respectively. We present the speed of waves for in-plane particle motion computed from (6) along with the actual values. The theoretical and PINN inferred values of v_{p_1} are $5.27 \text{ mm}/\mu\text{s}$ [10] and $5.29 \text{ mm}/\mu\text{s}$, respectively. This gives a relative error of 0.3%. However a relative error of 2.6% is observed for v_{s_1} with actual and PINN inferred value being $2.30 \text{ mm}/\mu\text{s}$ and $2.23 \text{ mm}/\mu\text{s}$, respectively. We also present the values of c_{11} and c_{12} in Table I, which are computed from PINN. Table I also shows the actual values c_{11} and c_{12} and L^2 - relative error between actual and PINN computed value for single-crystal Nickel. The relative errors are very small and amount to 3% and 4% for c_{11} and c_{12} , respectively.

B. PINN for polycrystalline Nickel

Next, we show the capabilities of PINN in inferring \hat{c}_{44} with the experimental wavefield data measured as u_2 . The computation of \hat{c}_{44} is carried out for wavefield data acquired with $[400 \times 400]$ and $[50 \times 50]$ grids in space. A total of 120 time snapshots, representing wavefield data from $2 \mu\text{s}$ to $4.42 \mu\text{s}$, are selected.

Thereafter, 12.5% of time snapshots are selected in the temporal domain and 20% data points were sampled spatially in each time snapshot using an *i.i.d.* approach. Choosing the optimal hyper-parameters is important for the convergence of neural network training. A more sophisticated meta-learning approach can be used to obtain the best hyper-parameters of the networks, but due to high computational cost associated with it, we choose the network architecture based on the complexity of the data and our past experience with PINNs. Nevertheless, Table II gives the maximum and minimum values of c_{44} and v_{s_2} for the polycrystalline Nickel obtained using different width and depth of the networks. Table II clearly shows that parameters become consistent for depth and width of 6 and 50, respectively. Therefore, the hyper-parameters used in this study can be considered as adequate if not optimal.

Figure 5a shows a time snapshot of u_2 at $t = 3.84 \mu s$ and overlaid with red solid dot representing the samples chosen for training of PINN. Subsequently, PINN simulations are performed with hyper-parameters shown in Table III. Figure 5b shows the comparison between actual and PINN simulated data along for $x_3 = 2 \text{ mm}, 4 \text{ mm}, 6 \text{ mm},$ and 8 mm represented by lines in black, yellow, blue and magenta colors in Figure 5a, respectively. Figure 5b shows a very good agreement between actual and PINN simulated solutions. Figure 5c shows the spatial variation of v_{s_2} in a range of $[2.95 \text{ mm}/\mu s, 3.00 \text{ mm}/\mu s]$ ensuring the change in stiffness of crystals properties, especially rigidity (c_{44}). We note that for a homogeneous single-crystal Nickel, the speed of v_{s_2} is $2.97 \text{ mm}/\mu s$ [18]. Figure 5d shows the variation c_{44} of the polycrystalline Nickel, which varies from 79 GPa to 82 GPa and conforms with the v_{s_2} as low and high speeds correspond to low and high value c_{44} .

Next, we compute the uncertainty in the $v_{s_2}(\hat{c}_{44})$ by using the wavefield data for u_2 acquired with $[50 \times 50]$ grid points in space. To perform the PINN simulation we utilized unfiltered PCA data comprising 120 time snapshots from $2 \mu s$ to $4.42 \mu s$ and sampled with a rate of 12.5% in the temporal domain and 60% in the spatial domain. The slow convergence of PINN due to presence of noise in the data is circumvented by the approach of weight decay [19], which eventually bounds the weights of neural network, hence resulting in a faster convergence. Therefore, the loss function in equation (10) is further modified and expressed as

$$J_{\hat{c}_{44}}(\Theta) = \lambda_{u_2} MSE_{u_2} + \lambda_{f_2} MSE_{f_2} + \underbrace{\lambda_w \|\mathbf{w}\|_2^2}_{\text{Weight decay}}. \quad (15)$$

The PINN for u_2 is executed five times with different initialization of parameters of neural network and optimized loss function as defined in (15). The values of λ_{u_2} , λ_{f_2} , and λ_w are taken as 50, 5, and 0.1, respectively. The standard deviation and mean of minimum and maximum value of v_{s_2} , inferred from the PINNs, are $(3 \times 10^{-3} \text{ mm}/\mu s, 4 \times 10^{-4} \text{ mm}/\mu s)$ and $(2.9831 \text{ mm}/\mu s, 2.9845 \text{ mm}/\mu s)$. The small standard deviation confirms the consistency of the simulations carried out by the PINNs. Additionally,

due to coarse sampling, the speed of v_{s_2} observed from this data set does not show large spatial variation as it is not able to capture the fine variation of grains.

VI. SUMMARY

In this study, we quantified the microstructure as defined by elements of stiffness tensor (\hat{c}_{ij}), of a cubically symmetric polycrystalline Nickel. The (\hat{c}_{ij}) are inferred by using the physics-informed neural network (PINN) trained with the ultrasonic wavefield dataset acquired at the frequency of 5 MHz. The PINNs are informed with two sets of decoupled second order hyperbolic partial differential equations, each defining the in-plane and out-of-plane particle displacement, respectively. Data of particle displacements are recorded in a spatio-temporal way and represented by three orthogonal components of displacement; u_1 and u_3 for in-plane and u_2 for out-of-plane motion. We validate the efficacy of PINNs by first computing the \hat{c}_{ij} for a single-crystal and polycrystal Nickels. For a single-crystal Nickel, a shallow network of two hidden-layers produced very accurate estimations of \hat{c}_{11} and \hat{c}_{12} (represented by speeds of longitudinal (v_{p_1}) and first shear waves (v_{s_1}), respectively). Subsequently, PINNs are implemented for polycrystal Nickel and trained with experimental datasets representing u_2 . We used two experimental wavefield imaging datasets acquired at different spatial resolutions of 400×400 and 50×50 grid points. A comparison between actual and PINNs simulated data shows a very good agreement and spatial variation of \hat{c}_{44} (representing v_{s_2} , speed of second shear wave) shows presence of polycrystal of different stiffness. We used the second dataset acquired at 50×50 grid points to compute the uncertainty and consistency of PINNs. A very small standard deviation in minimum and maximum v_{s_2} proves the consistency of PINNs. All the above computational experiments have used a very small fraction of data in space (40% and 20%) and time (12.5%).

In this work we have used an *i.i.d.* approach for sampling the data points. However, there are other approaches like importance sampling that can be used with sparse dataset. In this study, a generic representation of PINNs works very accurately but we observed a slow convergence for some high frequencies, which is generally caused by *spectral bias* [20] phenomena present in the neural network. Therefore, the future scope of work will include embedding the input variables (\boldsymbol{x}) in Fourier space and performing the training through Fourier feature mappings corresponding to individual frequencies [21]. Additionally, we presented the quantification of microstructure based on the 2D wavefield datasets for a single ultrasonic frequency. Future ongoing work will include extension of the current work for 3D datasets acquired for various frequencies.

ACKNOWLEDGMENTS

The work was supported by OSD/AFOSR MURI Grant FA9550-20-1-0358, DOE PhILMs project (DE-SC0019453) and the DURIP Grant W911-NF-2110089. This research was conducted using computational resources and services at the Center for Computation and Visualization (OSCAR), Brown University, Oak Ridge National Lab (ORNL) and Longhorn machine of Texas Advanced Computing Center's (TACC). KS would like to acknowledge Dr. Helen Kershaw of NCAR, Colorado, for providing help with problems concerning the computation.

REFERENCES

- [1] H. Ledbetter *Sound velocities and elastic-constant averaging for polycrystalline copper*, Journal of Physics D: Applied Physics, 13, 1879-1884 (1980)
- [2] H. Seiner, L. Bodnarova, P. Sedlak, M. Janecek, O. Srba, R. Kral, and M.Landa, *Application of ultrasonic methods to determine elastic anisotropy of polycrystalline copper processed by equal-channel angular pressing*, Acta Mater, 58(1), 235–247 (2010).
- [3] M. Raissi, P. Perdikaris, and G. Karniadakis *Physics-informed neural networks: A deep learning framework for solving forward and inverse problems involving nonlinear partial differential equations*, Journal of Computational Physics, 378 (2019): 686-707.
- [4] A. Baydin, B. Pearlmutter, A. Radul, and J. Siskind, *Automatic differentiation in machine learning: A survey* The Journal of Machine Learning Research, 18(1), pp.5595-5637 (2017).
- [5] K. Shukla, P. Leoni, J. Blackshire, D. Sparkman and G. Karniadakis *Physics-Informed Neural Network for Ultrasound Nondestructive Quantification of Surface Breaking Cracks*, J Nondestruct Eval 39, 61 (2020).
- [6] A. D. Jagtap, K. Kawaguchi, and G. E. Karniadakis, *Adaptive activation functions accelerate convergence in deep and physics-informed neural networks*, Journal of Computational Physics, 404, 109136 (2020).
- [7] A. D. Jagtap, K. Kawaguchi, and G. E. Karniadakis, *Locally adaptive activation functions with slope recovery for deep and physics-informed neural networks*, Proceedings of the Royal Society A 476 (2239), 20200334, 2020.
- [8] J. Blackshire, and S. Sathish, *Near-field ultrasonic scattering from surface-breaking cracks.*, Applied Physics Letters, 80, no. 18, p.3442 (2002).
- [9] A. D. Jagtap, Y. Shin, K. Kawaguchi, G.E. Karniadakis, *Deep Kronecker neural networks: A general framework for neural networks with adaptive activation functions*. arXiv preprint, arXiv:2105.09513, 2021.
- [10] Y. Xu, T. Aizawa and J. Kihara, *Simultaneous determination of elastic constants and crystallographic orientation in coarse-grained nickel by acoustic spectro-microscopy*, Materials transactions, JIM, 38, no. 6, p.536 (1997).
- [11] S. Sathish, M. Mendik, J. Cantrell and W. Yost, *Elastic constants and crystal orientation of individual grains of polycrystalline solids from scanning acoustic microscopy*, The Journal of the Acoustical Society of America, 98, no. 5, p.2854 (1995).
- [12] C. Kube, and J. Turner, *Ultrasonic attenuation in polycrystals using a self-consistent approach*, Wave Motion, 57, p.182 (2015).
- [13] M. Norouziyan, and J. Turner, *Ultrasonic wave propagation predictions for polycrystalline materials using three-dimensional synthetic microstructures: Attenuation*, The Journal of the Acoustical Society of America, 145, no. 4, p.2181 (2019).

- [14] M. Mendik, S. Sathish, A. Kulik, G. Gremaud and P. Watcher, *Surface acoustic wave studies on single-crystal nickel using Brillouin scattering and scanning acoustic microscope*, Journal of applied physics, 71, no. 6, p.2830 (1992).
- [15] J. Carcione, *Wave fields in real media: Wave propagation in anisotropic, anelastic, porous and electromagnetic media*, Elsevier (2014).
- [16] M. Groeber and M. Jackson, *SDREAM.3D: A digital representation environment for the analysis of microstructure in 3D*, Integrating materials and manufacturing innovation, 3, no. 1, p.56 (2014).
- [17] A. Migliori and Z. Fisk, *Crystals and ultrasound, old-fashioned materials science*, Los Alamos Science, no. 21, p.182 (1993).
- [18] Dakota Ultrasonics Velocity Table, <https://dakotaultrasonics.com/reference/> accessed on: 2021-03-10.
- [19] K. Nakamura and W-B. Hong, *Adaptive weight decay for deep neural networks*, IEEE Access, no. 7, p.118857 (2019).
- [20] S. Wang, H. Wang and P. Perdikaris, *On the eigenvector bias of Fourier feature networks: From regression to solving multi-scale PDEs with physics-informed neural networks*, arXiv preprint, arXiv: 2012.10047 (2020).
- [21] B. Wang, W. Zhang and W. Cai, *Multi-scale deep neural network (mscalednn) methods for oscillatory stokes flows in complex domains*, arXiv preprint, arXiv:2009.12729 (2020).
- [22] N. Rahaman, D. Arpit, A. Baratin, F. Drexler, M. Lin, F. Hamprecht, Y. Bengio and A. Courville, *On the Spectral Bias of Deep Neural Networks*, In International Conference on Machine Learning, PMLR, pp. 5301-5310 (2019).

Khemraj Shukla is an Assistant Professor (Research) in the Division of Applied Mathematics at Brown University, USA. His research focuses on the development of scalable codes on heterogeneous computing architectures.

Ameya D. Jagtap is an Assistant Professor of Applied Mathematics (Research) in the Division of Applied Mathematics at Brown University, USA. His research focuses on the intersection of machine learning and computational physics.

James L Blackshire is a Senior Research Engineer and Senior Material Scientist at the Wright-Patterson Air Force Research Laboratory, based out of Ohio, USA.

Daniel Sparkman is a Scientist at Wright-Patterson Air Force Research Laboratory, based out of Ohio, USA.

George Em Karniadkais is the Charles Pitts Robinson and John Palmer Barstow Professor of Applied Mathematics and Engineering at Brown University, USA, and he has a joint appointment with PNNL, where he is the Director of the PHILMs Collaboratory on physics-informed learning.